"Magnetic behavior of nanofilms prepared by assembling different Co ferrite nanoparticles"

Viviana B. Daboin[a], Julieta S. Riva[a], Paula G. Bercoff[b] [*].

[a] CONICET, Instituto de Investigaciones en Fisicoquímica de Córdoba (INFIQC). Universidad Nacional de Córdoba, Facultad de Ciencias Químicas, Ciudad Universitaria, X5000HUA Córdoba, Argentina.
[b] CONICET, Instituto de Física Enrique Gaviola (IFEG). Universidad Nacional de Córdoba, Facultad de Matemática, Astronomía, Física y Computación, Ciudad Universitaria, X5000HUA Córdoba, Argentina.

*paula.bercoff@unc.edu.ar

Abstract

We study the magnetic characteristics of nanofilms composed of $CoFe_2O_4$ nanoparticles synthesized using thermal decomposition (TD) and self-combustion (SC) methods, assembled on glass substrates using the Langmuir-Blodgett technique. Despite both synthesis methods render crystalline Co ferrite nanoparticles, the differences in particle size and saturation magnetization are notable; however, both nanofilms reveal a ferrimagnetic behavior and display a significant surface contribution to the net magnetization at temperatures below 50 K. This effect is attributed to the nanoparticles' surface spins misaligning with the spins of the ordered core and freezing into a disordered structure. Effective anisotropy K_{eff} values were determined, obtaining similar values to the bulk material (K_{eff} ~$2x10^5$ J/m^3) for the nanofilm made of TD nanoparticles, while the nanofilm prepared with SC nanoparticles presents an enhanced value (K_{eff}=$5x10^5$ J/m^3). The temperature-dependent saturation magnetization curves were fitted with the modified Bloch's law and an additional term that corresponds to the frozen spins.
.

1. Introduction

In the last decades, $CoFe_2O_4$ nanoparticles (NPs) have received immense interest from scientists due to their magnetic properties such as high magnetocrystalline anisotropy, high coercivity, moderate saturation magnetization, high specific electrical resistance, and magnetoelastic effect [1]. Due to these properties, $CoFe_2O_4$ NPs with appropriate surface chemistry can be employed in numerous biomedical applications as contrast agents to improve magnetic resonance imaging quality, magnetic carriers for drug delivery, hyperthermia therapy or industrial process engineering, being promising for applications such as sensors, magnetic storage devices, microwaves, solar cells, and electrical devices [2,3].

The size distribution of Co ferrite NPs [4], their morphology [5], the packing density [6], the intergranular exchange interaction [7], and the distribution of cations [8] are some of the factors that are responsible for their magnetic properties. Among these, grain/particle size and their distributions are some of the most important factors governing the magnetic properties of nanomaterials. Therefore, it is clear that microstructure manipulation of these NPs allows customizing their physical attributes, which is possible using different synthesizing methods [1].

Thermal decomposition is a synthetic method that allows obtaining spherical and highly monodisperse NPs functionalized by organic molecules and stabilized in an organic solvent. This method has been widely employed for the synthesis of $CoFe_2O_4$ NPs, varying the precursors. For example, Randhawa et al. have reported the thermal decomposition of cobalt tris(malonato) ferrate(III) trihydrate at 380° C [9]. Also, Carp et al. have reported the synthesis of $CoFe_2O_4$ NPs by the decomposition of polynuclear coordination compounds at 350 °C - 450 °C [10]. On the other hand, Hashemi et al. have reported the synthesis of $CoFe_2O_4$ NPs by the decomposition of $[Co(en)_3Fe(ox)_3]$ at 400 °C [11], and Dimpal Tomar et al. have obtained $CoFe_2O_4$ NPs by the decomposition of Co-Fe glycolates as precursors [5]. Also,

surfactants have often been used to manipulate the size and morphology of the $CoFe_2O_4$ NPs. Typical compounds used in thermal decomposition are Fe and Co acetylacetonate complexes, and the surfactants are usually oleylamine and oleic acid [12,13]. By varying the synthesis conditions (temperature, time and volume of the solvent) different morphologies are obtained, such as nanospheres, nanocubes and nanohexagons. The disadvantage of this technique is the complex process, expensive starter chemicals, and low production quantities [14].

The synthesis process of the self-combustion method has many advantages, such as low cost, short reaction time, and the production of large amounts of material [14]. Organic compounds such as urea [14], glycine [15], citric acid [1], oxalyl dihydrazide [16], alanine or a mixture of them [17] are commonly used as fuel substances in the combustion method to increase the efficiency of the synthesis process. In synthesizing metal oxide NPs by the self-combustion method, predetermined stoichiometric ratios of metal nitrate salts and fuel are combined and then heated to approximately 400 °C to trigger exothermic reactions between the metal nitrates and the fuel [14].

In recent years, the interest in the use of NP arrays has increased, due to possible practical applications such as next-generation high-density perpendicular magnetic recording media [18], sensors, electronic logic devices [19], or magneto-optical devices [23], as well as in the investigation of fundamental magnetic properties. Therefore, the techniques to integrate NPs, allowing the formation of dense particle films with minimal defects, represent a crucial area of fundamental research. Progress in this field could greatly enhance the development of next-generation quantum devices [18], since defect-free films are critical for applications where precision is key. Among the numerous methods documented for the two-dimensional assembly of nanoparticles, the Langmuir–Blodgett (LB) technique stands out as the most versatile technique to obtain homogenous thin films of controlled thickness [18,19].

In the present paper, we report the preparation and characterization of $CoFe_2O_4$ NPs obtained by two different synthesis methods (thermal decomposition and self-combustion) and the preparation of nanofilms using the LB strategy with these NPs. Characterizing magnetic films is important for understanding their magnetic properties, such as magnetic susceptibility, coercivity, and saturation magnetization, which are essential for applications in data storage, sensors and quantum devices. A complete characterization also helps to predict how magnetic films will behave under different conditions (e.g., temperature, external magnetic fields), which is vital for reliable performance in practical applications. Here, the morphology, crystal structure, and magnetic properties of the materials were evaluated. The magnetic nanofilms were characterized by scanning electron microscopy (SEM), atomic force microscopy (AFM), and magnetometry, applying the external field both in plane (IP) and out of the substrate's plane (OoP). A magnetic easy plane was found, indicating a planar effective anisotropy in both nanofilms. We find that the effective anisotropy constant K_{eff} is enhanced in the nanofilm prepared with the nanoparticles synthesized by self-combustion. This is possibly because they are larger (and surface spins are less dominant) and because their saturation magnetization largely exceeds that of the nanoparticles prepared by thermal decomposition. A detailed understanding of magnetic films can lead to new discoveries and innovations in various fields, including electronics, medicine, renewable energy, and enhancing existing technologies.

2. Materials and methods

2.1 Synthesis of Co ferrite NPs by self combustion

Cobalt ferrite NPs ($CoFe_2O_4$) were synthesized using the self-combustion method, as previously described [20]. CoC_2O_4, $Fe(NO_3)_3$, and citric acid were used as precursors for the preparation, and all materials were utilized without further purification. In short, iron nitrate and cobalt oxalate were dissolved in 50 ml of water, maintaining a constant stoichiometric ratio ([Fe(III)] + [Co(II)] = 1 M). A 3 M citric acid solution (50 ml) was added to the solution and heated at 40 °C for 30 min with vigorous stirring. The final mixture slowly evaporated until a highly viscous gel was formed. This gel was then heated below 200 °C, initiating a self-propagating combustion process. The self-propagating combustion lasts until the gel is completely carbonized, thus generating a powder. Finally, the powder samples were calcined at 800 °C for 2 h.

The obtained powder was modified with stearic acid (SA) following the procedure described elsewhere [21]. For this, 0.15 g of NPs were first

dispersed in a mixed solution of 25 ml absolute ethanol and 0.075 g stearic acid. The resulting solution was immersed in an ultrasonic bath at 80°C for 1 h. Then, the resulting mixture was washed 5 times to remove the free stearic acid and it was finally dried at 60°C for 24 h. The modified $CoFe_2O_4$ NPs so-obtained were labeled Co-P-SC.

2.2 Synthesis of Co ferrite NPs by thermal decomposition

Cobalt ferrite nanoparticles were also synthesized using the thermal decomposition method (TD) [13, 22] with commercially available reagents without further purification. The procedure involved mixing 2 mmol of Fe(acac)$_3$, 1 mmol of Co(acac)$_2$, 10 mmol of hexadecanediol, 6 mmol of oleic acid (OA), 6 mmol of oleylamine, and 20 ml of benzyl ether. The reaction mixture was magnetically stirred in the presence of nitrogen gas at room temperature for 60 min, then heated to 100 °C for 30 min to remove the water. Subsequently, the temperature was increased to 200 °C for 30 minutes to facilitate nucleation, and then it was raised to 280 °C for 60 min to promote the NPs growth. Ethanol was added to the mixture under ambient conditions, resulting in the precipitation of a black material, which was then collected using a magnet. Finally, the obtained NPs were dried overnight in an oven at 60 °C for their preservation and subsequent use. The NPs synthesized by this method were coated with oleic acid and they were labeled Co-P-TD.

2.3 Preparation of nanofilms

The transfer of Co-P-SC and Co-P-TD onto glass substrates was performed using the Langmuir-Blodgett method, following a procedure similar to one previously reported [23]. The pressure-area isotherms of nanofilms at the air/water interface were monitored with a Wilhelmy plate on a KSV Mini-trough (36.4 cm x 7.5 cm, KSV model 2000). To transfer Co-P-DT to the glass, a 1.5 mg/ml solution was prepared using a mixture of chloroform and methanol as the solvent. Then, 150 µl of the suspension was spread at the air/water (Milli-Q, 18.2 MΩ, Millipore) interface using a micro-syringe. Compression of the film was done at a rate of 10 mm/min after the solvent evaporated (approximately 20 min). The formed films were transferred at a pressure of 40 mN/m onto a glass

substrate at a rate of 3 mm/min. The glass substrates were previously washed several times with acetone, ethanol, and Milli-Q water, and then treated with hexane. The so-obtained nanofilm is named Co-F-TD. The deposition of Co-P-SC on a glass substrate was carried out using the same procedure and conditions mentioned above, with the difference that 300 µl of a solution with a concentration of 5 mg/ml was employed. This latter nanofilm is named Co-F-SC.

2.4 Experimental Techniques

Both kinds of NPs (Co-P-SC and Co-P-TD) and nanofilms (Co-F-SC and Co-F-TD) were characterized by different techniques. The crystal structure was identified by using X-ray powder diffraction (XRD) with a PANalitycal X'Pert Pro diffractometer using Bragg-Brentano geometry, operated at 40 kV, 40 mA, Cu Kα radiation (λ= 1.5418 Å) and with a step size of 0.02°, from 10° to 80°. The morphology of NPs and films was determined using a Sigma Zeiss Field Emission Scanning Electron Microscope (FE-SEM), a transmission electron microscope Zeiss (Leo 906E), and an Atomic Force Microscope (AFM) Agilent Technologies 5500. AFM measurements were performed in tapping mode at atmospheric pressure and room temperature by using a rotated monolithic silicon probe coated with an aluminum reflex film (Budget Sensors TAP150-Al-G, Nominal spring constant 5 N/m, resonance frequency of 150 kHz, nominal radius < 10 nm). Magnetic characterization of the NPs and nanofilms was conducted with a Cryogenic Ltd. vibrating sample magnetometer (VSM) with maximum fields of ±5 T at different temperatures.

3. Results

3.1 NPs characterization

Figure 1 shows the results of the structural and magnetic characterization of Co-P-SC and Co-P-TD. Figure 1(a) displays a SEM image of Co-P-SC, while Figure 1(b) is the TEM image of Co-P-TD. When comparing these images, it can be seen that both kinds of NPs do not exhibit a perfectly spherical morphology. Mean diameters of (84 ± 2) nm for Co-P-SC and (12 ± 1) nm for Co-P-TD could be determined, as shown in the superimposed histograms in Figure 1(a) and 1(b). The size distribution of Co-P-TD is

smaller when compared to the corresponding to Co-P-SC, since the thermal decomposition method allows obtaining smaller and monodisperse particles [24].

X-ray diffraction patterns of Co-P-SC and Co-P-TD are presented in Figure 1(c). The peak positions, corresponding to reflections (2 2 0), (3 1 1), (2 2 2), (4 0 0), (4 2 2), (3 3 3), (4 4 0), (5 3 1), (6 2 0), (5 3 3), (6 2 2), and (4 4 4) match well with the standard diffraction peaks of the cubic spinel structure (JCPDS-PDF 22-1086), which is characteristic of cobalt ferrite, confirming that no other phases are present. Additionally, the crystallite's average size was determined using the Scherrer equation, giving (80 ± 5) nm and (9 ± 2) nm for Co-P-SC and Co-P-TD, respectively. The diffraction peaks of Co-P-TD are broader and of lower intensity compared to those of Co-P-SC, which is attributed to the smaller crystallite size of Co-P-TD. This broadening, along with a reduction in peak intensity, is related to the smaller crystallites with fewer atomic planes contributing to the diffraction and a higher surface-to-volume ratio introducing imperfections [25, 26]. Finally, comparing the average crystallite diameters with the grain sizes measured by microscopy allows us to conclude that both types of nanoparticles are single crystals. Rietveld refinements of Co-P-SC and Co-P-TD X-ray diffraction patterns were performed, using the software XPert HighScore Plus (Malvern Panalytical) and they are presented in Figure S1(a) and S1(b) of the Supplementary Information. The lattice parameter a given by the refinements is $a = 8.40508(3)$ for Co-P-TD and $a = 8.3718(4)$ for Co-P-SC.
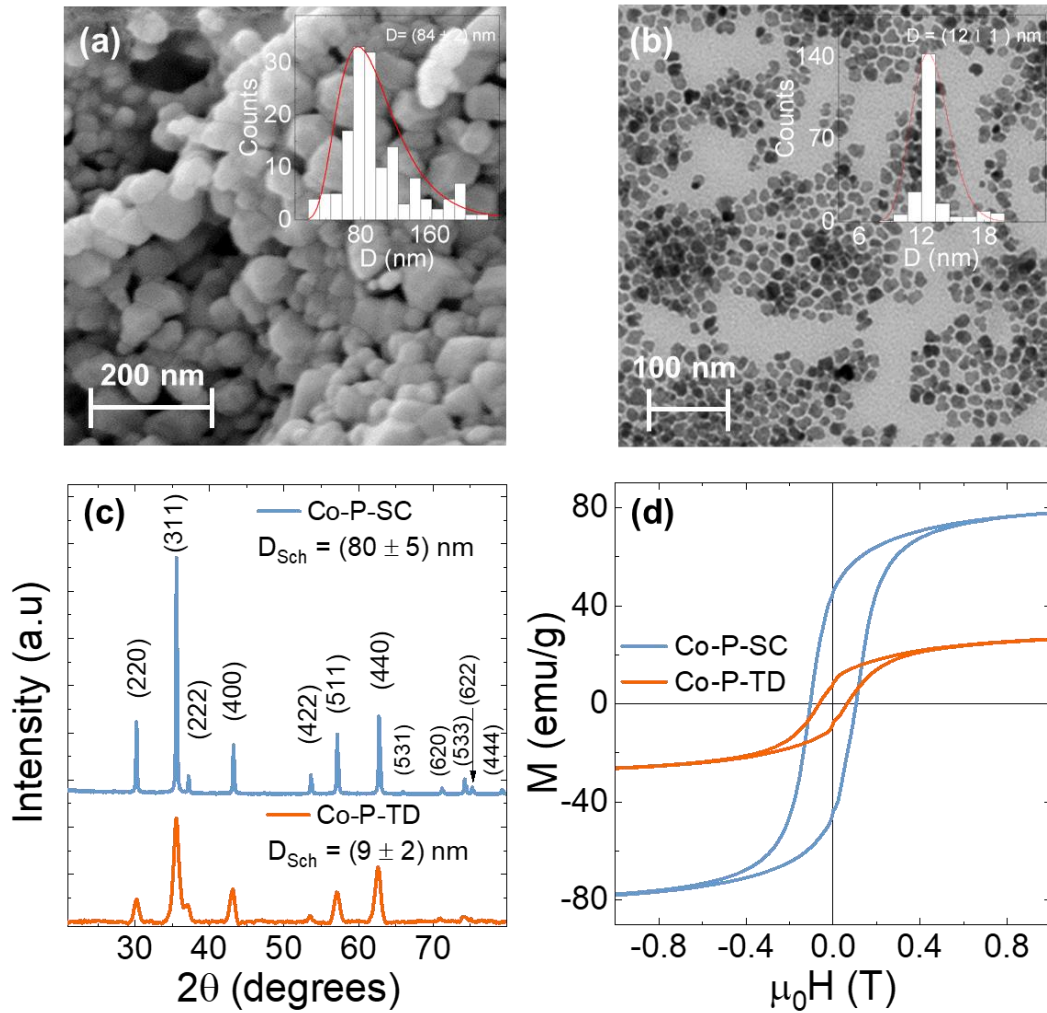

Figure 1. (a) SEM image and size histogram of Co-P-SC. (b) TEM image and size histogram of Co-P-TD. (c) XRD patterns and (d) hysteresis loops measured at 300 K of Co-P-SC (blue line) and Co-P-TD (orange line). The maximum applied field was ±5 T but only the ±1 T range is displayed, for the sake of clarity.

Figure 1 (d) shows the hysteresis loops of Co-P-SC and Co-P-TD measured at 300 K, after compacting the NPs in 5 mm diameter and 1 mm thin disks. A ferrimagnetic behavior is observed in both samples, with notable values of remanence (M_R) and coercivity (H_C). The saturation magnetization (M_S) values obtained for Co-P-SC and Co-P-TD were 84 emu/g and 33 emu/g, respectively. The M_S value for Co-P-SC falls within the range of bulk $CoFe_2O_4$ (between 80 emu/g and 85 emu/g) [27, 28]. However, sample Co-P-TD displays a much lower M_S value compared to Co-P-SC and bulk $CoFe_2O_4$. This discrepancy can be attributed to the smaller size of the Co-P-TD particles, resulting in a reduction in magnetization due to magnetic moment disorder at the NPs surface [29, 30], as well as the presence of non-magnetic oleic acid molecules adsorbed on the NPs surface [31]. Furthermore, the M_S value for Co-P-TD is comparable to that reported for $CoFe_2O_4$ NPs of similar size, prepared using the thermal decomposition method [13, 32]. It is important to note that the M_S values were calculated using the law of approach to saturation [33]. It is clear that although both synthesis methods produce crystalline $CoFe_2O_4$ NPs, significant differences in particle size and saturation magnetization are observed.

The H_C values obtained for samples Co-P-SC and Co-P-TD were 105 mT and 65 mT, respectively. This disparity arises from the strong dependence of coercivity on particle size. Typically, as particle size diminishes towards a critical diameter (D_C), an increase in coercivity is observed, reaching a peak before declining towards zero and becoming superparamagnetic [34]. Moreover, previous studies indicate a critical size of approximately 70 nm for $CoFe_2O_4$ NPs [35]. Consequently, it is expected that Co-P-SC NPs, with a mean diameter of 84 nm, will exhibit higher coercivity compared to Co-P-TD particles, which have a diameter of 12 nm and are close to the superparamagnetic limit.

On the other hand, Co-P-TD exhibits coercivity at room temperature (300 K), despite the expectation of superparamagnetic behavior for such small nanoparticles (12 nm). This phenomenon can be explained by several key factors. Firstly, the high magnetocrystalline anisotropy of cobalt ferrite significantly increases the energy barrier required to reverse the magnetization direction, overcoming the thermal effect that would induce superparamagnetism. Additionally, surface effects in nanoparticles of this size play an important role, as surface atoms experience greater anisotropy than those in the core, contributing to the retention of coercivity. Finally, the size of the particles places them in the single-domain regime, meaning that magnetization reversal involves overcoming the entire anisotropy energy barrier, resulting in measurable coercivity [36-38]. This combination of factors could explain why, despite their small size, the Co-P-TD nanoparticles retain coercivity at 300 K.

To further investigate the magnetic behavior of the nanoparticles, zero-field-cooling (ZFC) and field-cooling (FC) magnetization measurements were conducted. Both nanoparticle samples exhibit thermomagnetic irreversibility below the maximum measurement temperature of 350 K, as shown in Figures S2(a) and S2(b) of the Supplementary Information for Co-P-SC and Co-P-TD, respectively. The calculated blocking temperatures are 300 K for Co-P-SC and 270 K for Co-P-TD, which explain the samples' ferromagnetic behavior at and below these temperatures.

3.2 Pressure-Area Isotherms

Figure 2(a) presents the surface pressure-area isotherms measured for Co-P-SC (blue line) and Co-P-TD (orange line), aiming to identify the optimal conditions for transferring the NPs onto the substrate, assembling nanofilms. Initially, as the area decreases the surface pressure in both isotherms remains almost constant up to approximately 120 cm^2 for Co-P-TD and 140 cm^2 for Co-P-SC, which is characteristic of the gas phase in Langmuir-Blodgett films. Subsequently, a rapid increase in surface pressure occurs, indicating the formation of a solid phase and suggesting a closer packing of NPs, resulting in the formation of large organized domains of Co-P-SC and Co-P-TD. Notably, no collapse of the film is observed upon compression up to 55 mN/m and 67 mN/m for Co-P-SC and Co-P-TD, respectively. These isotherms confirm the successful formation of nanofilms at the air/water interface for both Co-P-SC and Co-P-TC.

Based on the surface pressure-area isotherms recorded for Co-P-SC and Co-P-TD, a pressure of 40 mN/m was determined as optimal for assembling the NPs onto a hydrophobic glass substrate (indicated by the dashed line in Figure 2(a)). This pressure ensures that the NPs are densely packed, forming a film. Additionally, as depicted in Figure 2(b), multiple

layers were transferred following the outlined procedure, with the maximum transfer ratio ranging between 1.4 and 0.3 for Co-P-SC and between 1 and 0.2 for Co-P-TD, during both ascending and descending movements of the substrates. The so-obtained nanofilms are named Co-F-SC and Co-F-TD when using Co-P-SC or Co-P-TD nanoparticles, respectively. Figure 2(c) schematically illustrates a nanofilm obtained using the Langmuir-Blodgett technique, indicating the in-plane (IP) and out-of-plane (OoP) directions used for magnetic characterization.
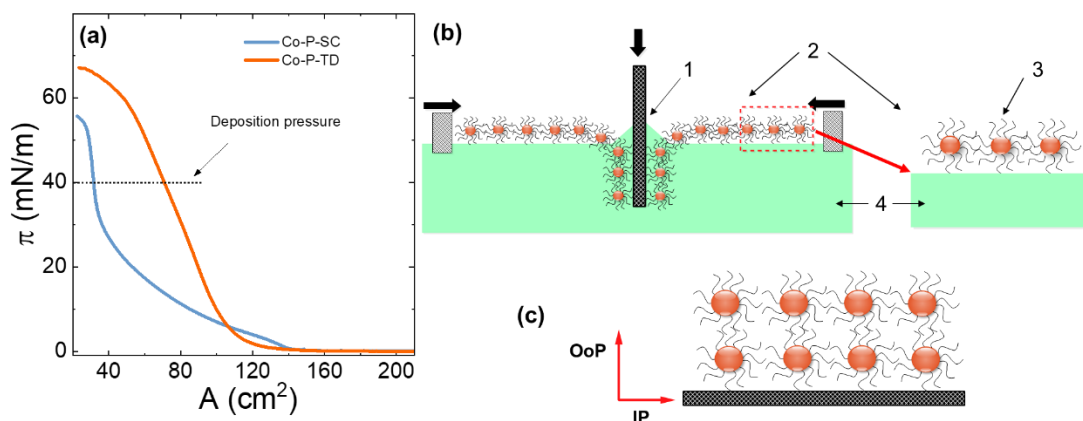

Figure 2: (a) Surface pressure versus area isotherm of Co-P-SC (blue line) and Co-P-TD (orange line) on a water subphase. (b) Schematic representation of the process for transferring a monolayer to a solid substrate: (1) substrate, (2) NP monolayer, (3) NP coated with oleic acid or stearic acid and (4) water subphase. (c) Illustration of the obtained nanofilm and the in-plane (IP) and out-of-plane (OoP) directions used for magnetic characterization.

3.3 Nanofilm characterization

The morphological characterization depicted in Figure 3 confirms the successful transfer of NPs onto the glass substrates. Analysis by AFM provides topographical details and cross-sectional profiles of the nanofilms Co-F-SC (Figure 3 (a), (b)) and Co-F-TD (Figure 3 (d), (e)). In the AFM images, bright regions correspond to NP agglomerates observed in both films. Cross-sectional profiles extracted from several AFM images reveal film thicknesses of 160 nm and 12 nm for Co-F-SC and Co-F-TD, respectively, suggesting that nanofilms are formed with approximately two layers of NPs in the case of Co-F-SC (with NP mean size of 84 nm) and one layer of NPs in the case of Co-F-TD (with NP mean size of 12 nm). This in turn shows that Co-F-TD has a smaller thickness than Co-F-SC as a result of the size difference between the different NPs used to obtain the films.

SEM images in Figure 3(c) and 3(f) depict the nanoparticle-assembled nanofilms at different scales. Notably, both nanofilms exhibit a high substrate coverage (>90% area), forming continuous layers across the substrate surface, as it can also be seen in Figures S3 and S4 of the Supplementary Information. Sample Co-F-SC displays less homogeneity compared to Co-F-TD, possibly because of lower Co-P-SC coverage with stearic acid, leading to greater NP agglomeration.
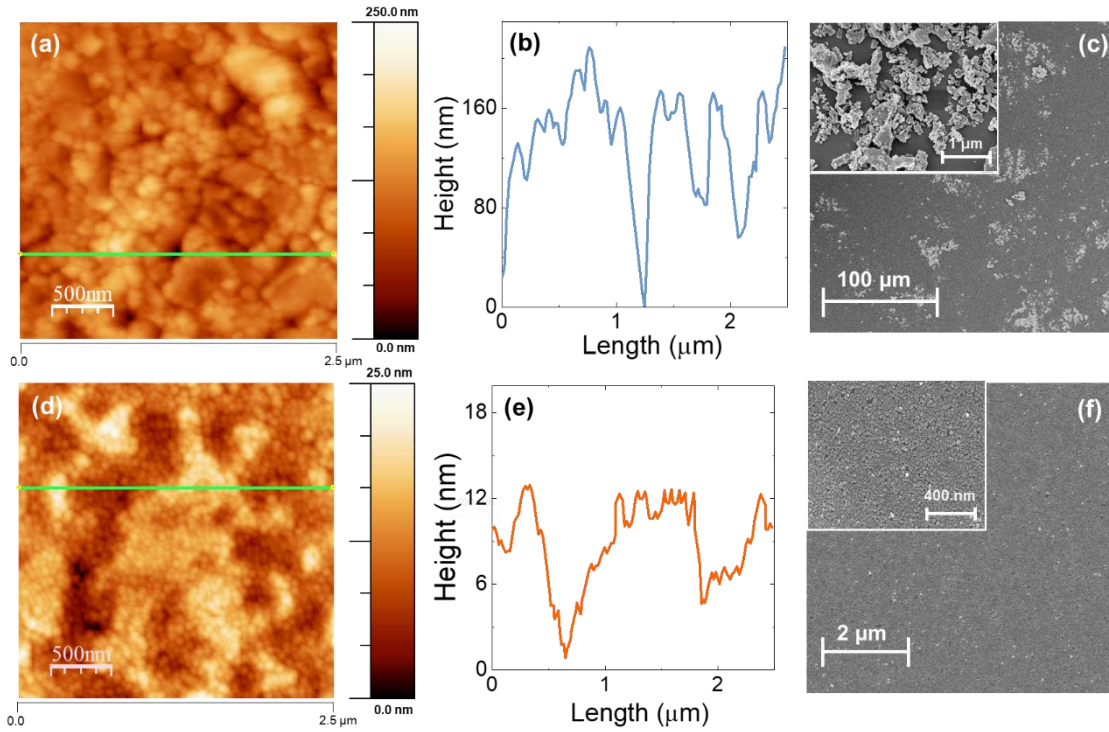
Figure 3. (a) AFM image, (b) cross-sectional line profile and (c) SEM images at different magnifications of nanofilm Co-F-CS. (d) AFM image, (e) cross-sectional line profile and (f) SEM images at different magnifications of nanofilm Co-F-TD.

3.4 Magnetic Properties of the nanofilms

Figure 4 displays the hysteresis loops measured at room temperature with the applied field in both in-plane (IP) and out-of-plane (OoP) directions of the nanofilms, as shown in Figure 2 (c). Despite the maximum applied field was ±5 T in every case, a smaller field range is displayed in Figure 4, for the sake of clarity. Diamagnetic contributions from the glass substrates have been subtracted from these hysteresis loops. When the magnetic field is applied in plane, saturation is achieved at lower saturation fields (Hs) compared to the OoP configuration, and a larger squareness (M_R/M_S) is observed IP for both nanofilms. Additionally, IP coercivity is higher when compared to the OoP direction. This behavior is consistent with a magnetic easy plane, which is usually preferred in 2-D nanostructures with strong shape anisotropy [39, 40]. The difference in H_C between the IP and OoP hysteresis loops is evident in both samples. However, this distinction is more pronounced in the Co-F-TD samples compared to Co-F-SC, which is attributed to the increasing film thickness diminishing the relevance of shape anisotropy [41]. The characteristic values of the hysteresis loops are summarized in Table 1.

Table 1. Magnetic parameters corresponding to the nanofilms: saturation magnetization Ms, remanent magnetization M_R, coercive field H_C, anisotropy field H_A and effective anisotropy constant K_{eff}.

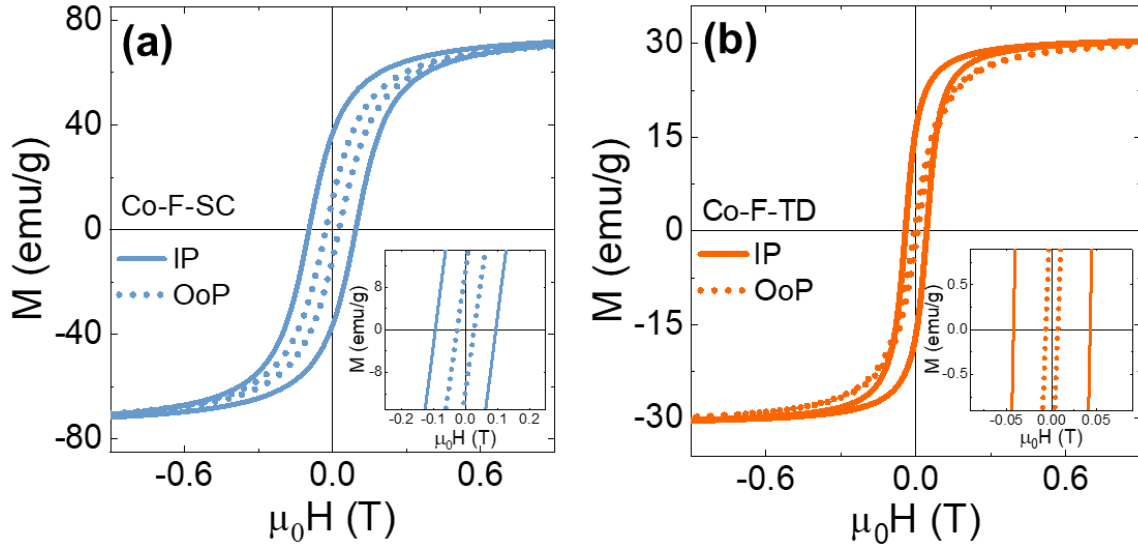| Sample	M_S (± 3 emu/g)	M_R (± 1 emu/g)		Hc (± 1 mT)		H_A (T)	K_{eff} (J/m³)
		IP	OoP	IP	OoP		
Co-F-SC	84	43	22	123	57	0.22	5 x 10⁵
Co-F-TD	33	17	2	43	7	0.24	2 x 10⁵

Figure 4. Hysteresis loops, measured at room temperature with the magnetic field applied IP and OoP for (a) Co-F-SC and (b) Co-F-TD. The insets are a zoom-in of the low-field region.

In magnetic films, various factors contribute to the effective anisotropy constant, K_{eff} including shape, magnetocrystalline and magnetoelastic anisotropies, as well as magnetostatic interactions, which vary depending on the specific system [42]. Several methods are available to estimate K_{eff} in a film, one of which involves calculating the difference in saturation fields, H_S, between the IP and OoP hysteresis loops. This difference provides a rough estimate of the anisotropy field, $H_A = H_S^{OoP} - H_S^{IP}$, from which the value of the K_{eff} can be obtained using the well-known expression $H_A = \frac{2K_{eff}}{M_S}$ [43]. However, for real systems a more accurate method to determine H_A is calculating the area in the first quadrant which is enclosed by the demagnetizing branches of the IP and OoP hysteresis loops [43]. Using this approach and the data from Figure 4, H_A values of 0.22 T for Co-F-SC and 0.24 T for Co-F-TD were obtained. Taking the Ms values for Co-F-SC and Co-F-TD as (4.44×10^6) A/m and (1.75×10^6) A/m, respectively, gives K_{eff} (Co-F-SC) = (5×10^5) J/m^3 and K_{eff} (Co-F-TD) = (2×10^5) J/m^3, at room temperature. These values are higher than $K_{eff} = (1.8 \times 10^5)$ J/m^3 obtained by M. H. Carvalho et al. for CoFe$_2$O$_4$–SiO$_2$ nanocomposites [44] and similar to the value for the bulk material K_{eff}

= (2×10^5) J/m^3 [45]. It should be noted that the K_{eff} value is higher for Co-F-SC than for Co-F-TD. As both nanofilms have a similar H_A, the difference in K_{eff} emerges from the difference in the Ms values. The K_{eff} for Co-F-TD is similar to the K_{eff} for the bulk material, even when the Ms for these nanoparticles is low. On the other hand, the K_{eff} for Co-F-SC is more than twice as that reported for the bulk material, even when the nanoparticles prepared by self-combustion have a Ms value similar to the bulk material. In order to further investigate this result, temperature dependent magnetization measurements were performed.

The IP magnetic hysteresis loops of Co-F-SC and Co-F-TD were measured at various temperatures ranging from 5 to 300 K. A comparison of the $M(H)$ curves at 5 K for both nanofilms is depicted in Figure 5(a). Notably, high coercive fields, as well as non-zero remanent and saturation magnetization, are observed. The magnetization curves of both nanofilms at 5 K exhibit the magnetic characteristics of CoFe$_2$O$_4$ nanoparticles below the blocking temperature [44].
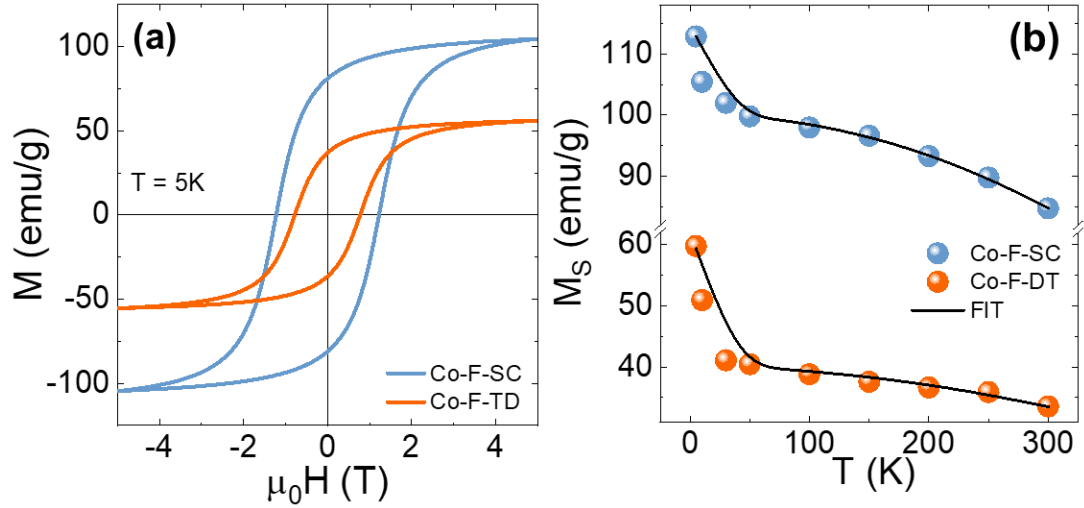
Figure 5. (a) Hysteresis loops at 5 K for both nanofilms, measured IP. (b) Saturation magnetization as a function of temperature for both nanofilms. Black solid lines correspond to fittings with Eq. (1).

The $Ms(T)$ values for both nanofilms were obtained from the hysteresis loops measured at different temperatures in the range of 5–300 K, using the law of approach to saturation [33] and are shown in Figure 5(b). From this figure, it is evident that a steep increase in Ms with decreasing temperature appears below 50 K, in both samples. This behavior is usually ascribed to a spin-glass-like behavior, and it can be modeled considering the modified Bloch law in addition to a surface spins contribution, as follows [1,50,51]:

$$M_S(T) = M_S(0)\left[1 - \left(\frac{T}{T_C}\right)^\alpha\right] + A\, e^{\left(-\frac{T}{T_f}\right)} \qquad (1)$$

where $M_S(0)$ is the saturation magnetization at 0 K, T_C is the Curie temperature, α is the Bloch's exponent (taking a value of 1.5 for bulk materials and between 1.5 and 3.0 for NPs [47–49]), A is the surface spin contribution and T_f is the surface spins freezing temperature.

Figure 5(b) shows the good agreement between the data and the fitting curve using Eq. (1) and Table 2 lists the parameters obtained from the fittings. The Bloch exponents for both samples are α=2 (greater than 1.5), as expected for interacting NPs. This large deviation from the ideal α value is the result of several finite size effects, such as an energy gap in the density of states for the spin waves and a lack of magnetic coordination at the surface [49]. In fact, a α=2 is expected for finite-size ferromagnetic clusters based on a mean field calculation [51,52].

The freezing temperatures T_f for Co-F-SC and Co-F-TD are (6±1) K and (10±1) K, respectively. Thus, the contribution of freezing spins to $Ms(T)$ is negligible above temperatures ~$5T_f$, similarly to how it was described for BiFeO$_3$–CuO nanocomposites [53].

Table 2. Fitting parameters to M_S(T) data using Eq. (1). $Ms(0)$ is the saturation magnetization at 0 K, T_C is the Curie temperature, α is the Bloch exponent and T_f is the freezing temperature.

Parameter	Co-F-SC	Co-F-TD
$Ms(0)$ [emu/g]	100±1	40±1
Tc [K]	750±60	770±50
α	2.0±0.2	2.0±0.4
A [emu/g]	30±3	32±2
T_f [K]	6±1	10±1

Coercivity values H_C at different temperatures for both nanofilms Co-F-SC and Co-F-TD are plotted in Figure 6.
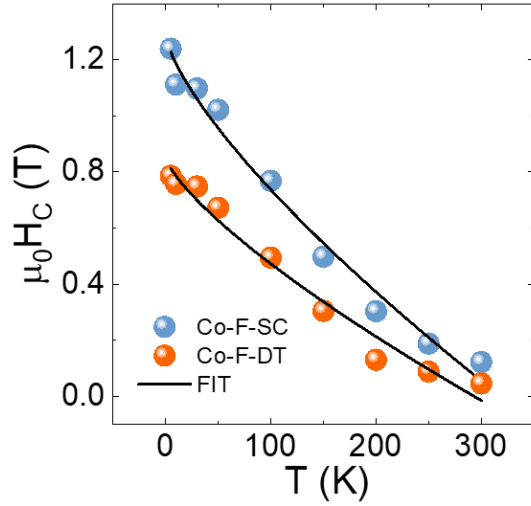

Figure 6. Coercivity as a function of temperature for Co-F-SC (blue symbols) and Co-F-TD (orange symbols) nanofilms. Black solid lines correspond to fittings with Eq. (2).

A systematic increase in coercivity is observed as the temperature decreases, indicating that the films become magnetically harder at lower temperatures [50]. The reason for the increasing coercivity with decreasing temperature can be understood by considering the effects of thermal fluctuations of the blocked moment across the anisotropy barrier [46]. In fact, the temperature dependence of H_C for all samples is found to closely follow the expression given by [1, 50]:

$$H_C = H_C(0) \left(1 - \frac{T}{T_B}\right)^\beta \quad (2)$$

where $H_C(0)$ is the coercivity at T = 0 K, T_B is the blocking temperature, and β is the exponent that usually takes the value of 0.5 for non-interacting single domains [50]. The fitting curves are plotted in Figure 6 as solid black lines, while the corresponding parameters are presented in Table 3. The exponents β vary between 0.7 and 0.8 in both samples and are indistinguishable within the error (see Table 3). Values of β closer to 1 are in agreement with predictions for the case of a collection of NPs with magnetic dipolar interaction [1]. T_B values are similar for both samples, being somewhat lower for Co-F-TD, in agreement with results obtained by Tomar et al. [5] for $CoFe_2O_4$ NPs synthesized by thermal decomposition. These authors also found that when the crystal size of the synthesized NPs decreases, the blocking temperature T_B is lower. On the other hand, the T_B value for sample Co-F-SC is similar to that obtained by Haïk Dunn et al. for similar $CoFe_2O_4$ NPs synthesized by the self-combustion method [20].

Table 3. Fitting parameters to H_C(T) data with Eq. (2). H_C (0) is the coercivity at $T = 0$ K, T_B is the blocking temperature, and β is the exponent.

Parameter	Co-F-SC	Co-F-TD
$H_C(0)$ [T]	1.3±0.1	0.9±0.1
T_B [K]	319±20	290±20
β	0.7±0.1	0.8±0.2

4. Conclusion

Cobalt ferrite NPs were prepared using the self-combustion and thermal decomposition methods. Two nanofilms on glass substrates were successfully prepared from these NPs using the Langmuir Blodgett technique. Film thicknesses of 160 nm for Co-F-SC and 12 nm for Co-F-TD were determined by AFM. The magnetic properties of the as-prepared films were investigated by measuring magnetization hysteresis curves over the 5 K to 300 K temperature range. A magnetic easy plane was found in both nanofilms, in agreement with a dominant planar shape anisotropy. In addition, a K_{eff} similar to the bulk material was obtained for sample Co-F-TD while an enhanced value of more than twice ($K_{eff} = 5 \times 10^5$ J/m³) was found for Co-F-SC, indicating that in this case, an optimal combination of particle size and the nanofilm

shape anisotropy contribute to the effective anisotropy.

The magnetic behavior of both nanofilms is described considering a model of a core-shell spin structure for the NPs, in which the core comprises magnetically ordered spins while the shell behaves as a spin-glass-like system. M_S(T) shows a sharp increase at temperatures below 50 K and it is described by the modified Bloch law with an additional exponential term accounting for spins freezing. The obtained freezing temperatures are T_f (Co-F-SC)=(6±1) K and T_f (Co-F-TD)=(10±1) K. The coercive field H_C decreases with temperature in both nanofilms, in agreement with NP systems with dipolar interaction, having both samples similar blocking temperatures around 300 K.

Conflict of Interest
The authors declare that they have no known competing financial interests or personal relationships that could have appeared to influence the work reported in this paper.

CRediT authorship contribution statement
Viviana B. Daboin: Data curation; Formal analysis; Investigation; Methodology; Validation; Visualization; Writing – original draft.
Julieta S. Riva: Conceptualization; Data curation; Formal analysis; Investigation; Methodology; Supervision; Validation; Visualization; Writing – original draft; Writing – review & editing.
Paula G. Bercoff: Conceptualization; Formal analysis; Funding acquisition; Investigation; Methodology; Project administration; Supervision; Validation; Visualization; Writing – review & editing.

Data availability
The data that support the findings of this paper are available from the corresponding author, upon reasonable request.

SUPPLEMENTARY INFORMATION

1. NPs characterization by X-ray diffraction

The crystal structure of the NPs was identified by X-ray powder diffraction (XRD) with a PANalitycal X'Pert Pro diffractometer using Bragg-Brentano geometry, operated at 40 kV, 40 mA, Cu Kα radiation (λ= 1.5418 Å) and with a step size of 0.02°, from 10° to 80°. X-ray diffraction patterns of Co-P-SC and Co-P-TD are presented in Figure S1(a) and S1(b) as well as the Rietveld refinements using the software *XPert HighScore Plus* (Malvern Panalytical). In both samples, the peak positions corresponding to reflections (2 2 0), (3 1 1), (2 2 2), (4 0 0), (4 2 2), (3 3 3), (4 4 0), (531), (620), (533), (622), and (444) match with the standard diffraction peaks of the cubic spinel structure, which is characteristic of cobalt ferrite (JCPDS-PDF 22-1086) and are shown in Figure 1c. The lattice parameters *a* obtained from the refinements are listed in Table S1. The diffraction peaks of Co-P-TD are broader and of lower intensity compared to those of Co-P-SC, which is attributed to the smaller crystallite size of Co-P-TD. Similar diffractograms with broad peaks were obtained by A. Zorai et al. for ultra-small cobalt ferrite synthesized by gamma irradiation [S1]. Because of the small size of the nanoparticles prepared by thermal decomposition, the XRD pattern is difficult to refine and converge to a closer fit between the measured data and the model. However, even when the goodness of fit obtained for Co-P-TD (Figure S1(b)) is not as good as that for Co-P-SC, the refinement is good enough to determine that the crystalline phase is the cubic spinel and that no secondary phases are present in this sample.

Table S1. Lattice parameter and crystallite size obtained from the refinements.

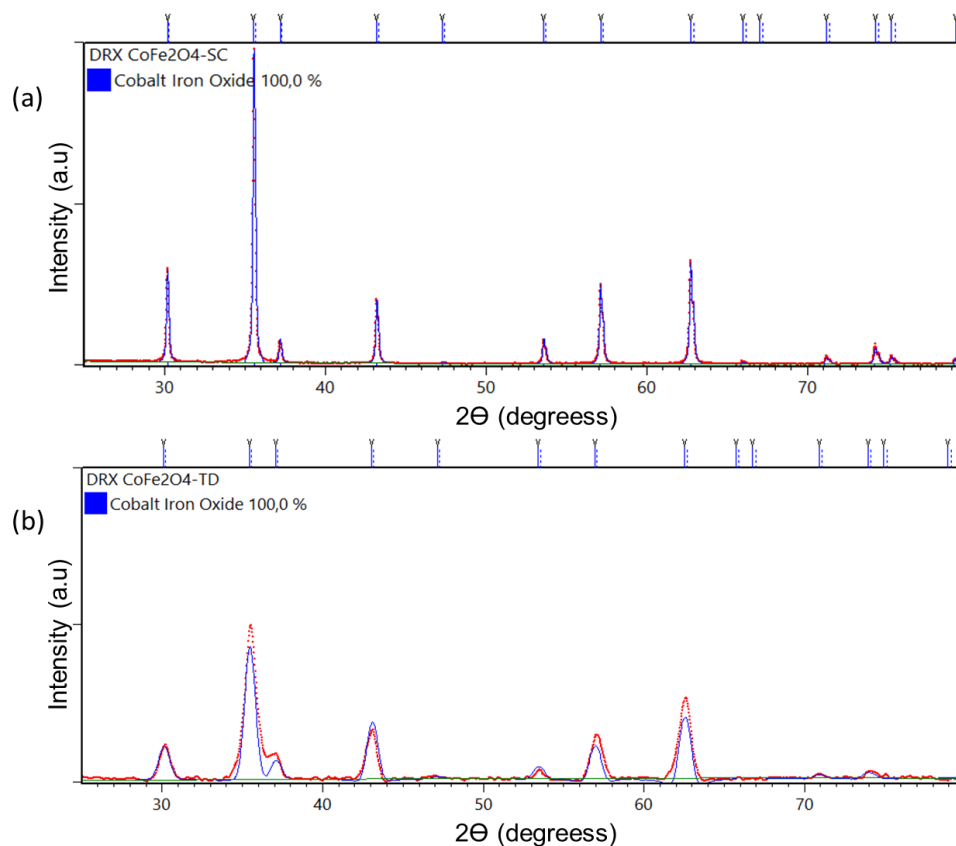| Sample	Lattice parameter *a* [Å]	Scherrer size [nm]
Co-P-TD	8.40508(3)	(9 ± 2)
Co-P-SC	8.3718(4)	(80 ± 5)

Figure S1. Rietveld refinement analysis of XRD patterns: (a) Co-P-SC and (b) Co-P-TD.

2. ZFC-FC curves

To further investigate the magnetic behavior of the nanoparticles, temperature dependent magnetization measurements were conducted from 5 K to 350 K, following the zero-field-cooling (ZFC) and field-cooling (FC) protocol. Both samples exhibit thermomagnetic irreversibility below 350 K, as it can be seen in Figure S2a and S2b for Co-P-SC and Co-P-TD, respectively. The blocking temperature (T_B) was determined by calculating the derivative of the difference between the ZFC and FC curves, (shown in the insets of Figure S4), being T_B=300K for Co-P-SC and T_B=270K Co-P-TD.

3. Nanofilm morphology

Figure S3 displays a SEM side view of the Co-F-SC nanofilm, where it is possible to distinguish a very good uniformity, indicating that the nanofilm is quite homogeneous in all its extension.

Due to the small thickness of the nanofilm Co-F-TD, a similar side image could not be observed by SEM. However, this nanofilm is very homogeneous, as it can be seen in the images displayed in Figure S4 taken from above, at different magnifications.

References

[S1] A. Zorai, A. Souici, D. Dragoe, et al., Superparamagnetic cobalt ferrite nanoparticles synthesized by gamma irradiation, *New J. Chem.*, 2023, 47, 2626.
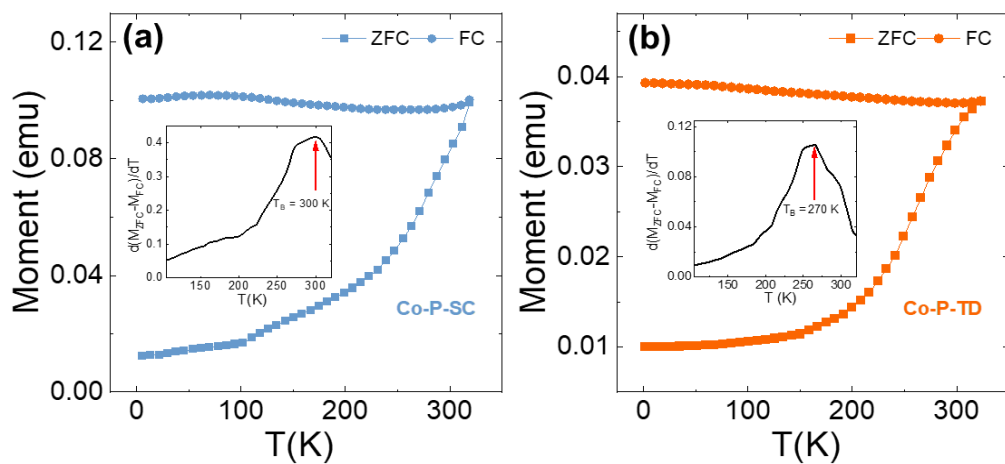
Figure S2: ZFC-FC curves for (a) Co-P-SC and (b) Co-P-TD. Insets: Blocking temperature distribution $\partial[M_{ZFC}-M_{FC}]/\partial T$.
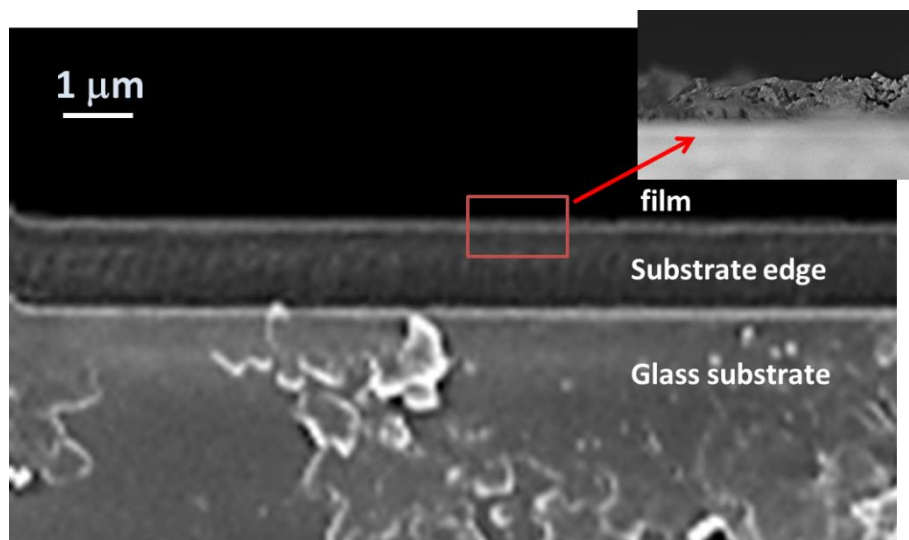

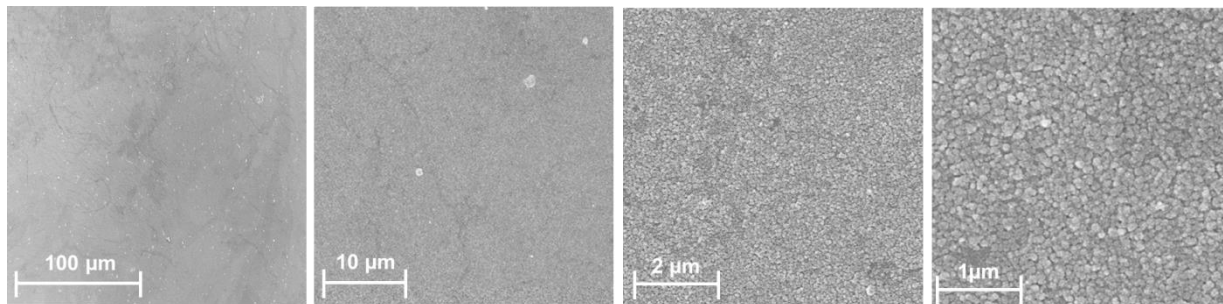Figure S3. Side view SEM images of the Co-F-SC nanofilm.

Figure S4. Top view SEM images of the Co-F-TD nanofilm.

References

[1]   E. Mosiniewicz-Szablewska, A.R. Clavijo, A.P.O.R. Castilho, L.G. Paterno, M.A. Pereira-Da-Silva, J. Więckowski, M.A.G. Soler, P.C. Morais, Magnetic studies of layer-by-layer assembled polyvinyl alcohol/iron oxide nanofilms, *Phys. Chem. Chem. Phys.* 20 **(2018)** 26696–26709. https://doi.org/10.1039/c8cp05404e.

[2]   S. Amiri, H. Shokrollahi, The role of cobalt ferrite magnetic nanoparticles in medical science, *Mater. Sci. Eng. C* 33 **(2013)** 1–8. https://doi.org/10.1016/j.msec.2012.09.003.

[3]   P.A. Vinosha, A. Manikandan, A.C. Preetha, A. Dinesh, Y. Slimani, M.A. Almessiere, A. Baykal, B. Xavier, G.F. Nirmala, Review on Recent Advances of Synthesis, Magnetic Properties, and Water Treatment Applications of Cobalt Ferrite Nanoparticles and Nanocomposites, *J. Supercond. Nov. Magn.* 34 **(2021)** 995–1018. https://doi.org/10.1007/s10948-021-05854-6.

[4]   I.C. Nlebedim, D.C. Jiles, Dependence of the magnetostrictive properties of cobalt ferrite on the initial powder particle size distribution, *J. Appl. Phys.* 115 **(2014)** 17A928. https://doi.org/10.1063/1.4867343.

[5]   D. Tomar, P. Jeevanandam, Synthesis of cobalt ferrite nanoparticles with different morphologies via thermal decomposition approach and studies on their magnetic properties, *J. Alloys Comp.* 843 **(2020)** 155815. https://doi.org/10.1016/j.jallcom.2020.155815.

[6]   K. Hiroi, H. Kura, T. Ogawa, M. Takahashi, T. Sato, Spin-glasslike behavior of magnetic ordered state originating from strong interparticle magnetostatic interaction in α-Fe nanoparticle agglomerate, *Appl. Phys. Lett.* 98 **(2011)** 252505. https://doi.org/10.1063/1.3602313.

[7]   J. Mohapatra, A. Mitra, D. Bahadur, M. Aslam, Superspin glass behavior of self-interacting $CoFe_2O_4$ nanoparticles, *J. Alloys Comp.* 628 **(2015)** 416–423. https://doi.org/10.1016/j.jallcom.2014.12.197.

[8]   D. Peddis, N. Yaacoub, M. Ferretti, A. Martinelli, G. Piccaluga, A. Musinu, C. Cannas, G. Navarra, J.M. Greneche, D. Fiorani, Cationic distribution and spin canting in $CoFe_2O_4$ nanoparticles, *J. Phys. Condens. Matter* 23 **(2011)** 426004. https://doi.org/10.1088/0953-8984/23/42/426004.

[9]   B.S. Randhawa, M. Gupta, M. Kaur, Preparation of cobalt ferrite from the thermolysis of cobalt tris(malonato)ferrate(III)trihydrate precursor, *Ceram. Int.* 35 **(2009)** 3521–3524. https://doi.org/10.1016/j.ceramint.2009.05.014.

[10]   O. Carp, L. Patron, A. Reller, Coordination compounds containing urea as precursors for oxides-A new route of obtaining nanosized $CoFe_2O_4$, *Mater. Chem. Phys.* 101 **(2007)** 142–147. https://doi.org/10.1016/j.matchemphys.2006.03.002.

[11]   M. Hashemi, F. Mohandes, M. Salavati-Niasari, A.S. Esmaeily, Preparation of cobalt ferrite micro/nanoparticles by solid-state thermal decomposition of a novel single-source precursor, *J. Mater. Sci. Mater. Electron.* 26 **(2015)** 6860–6867. https://doi.org/10.1007/s10854-015-3302-y.

[12]   Y. Eom, M. Abbas, H.Y. Noh, C.G. Kim, Morphology-controlled synthesis of highly crystalline Fe_3O_4 and $CoFe_2O_4$ nanoparticles using a facile thermal decomposition method, *RSC Adv.* 6 **(2016)** 15861–15867. https://doi.org/10.1039/c5ra27649g.

[13]   V. Daboin, S. Briceño, J. Suárez, G. Gonzalez, Effect of the dispersing agent on the structural and magnetic properties of $CoFe_2O_4/SiO_2$ nanocomposites, *J. Magn. Magn. Mater.* 451 **(2018)** 502–506.
https://doi.org/10.1016/j.jmmm.2017.08.043.

[14]   İ.H. Karakas, The effects of fuel type onto the structural, morphological, magnetic and photocatalytic properties of nanoparticles in the synthesis of cobalt ferrite nanoparticles with microwave assisted combustion method, *Ceram. Int.* 47 **(2021)** 5597–5609. https://doi.org/10.1016/j.ceramint.2020.10.144.

[15]   C.H. Yan, Z.G. Xu, F.X. Cheng, Z.M. Wang, L.D. Sun, C.S. Liao, J.T. Jia, Nanophased $CoFe_2O_4$ prepared by combustion method, *Solid State Commun.* 111 **(1999)** 287–291. https://doi.org/10.1016/S0038-1098(99)00119-2.

[16]   P. Bera, R. V. Lakshmi, B.H. Prakash, K. Tiwari, A. Shukla, A.K. Kundu, K. Biswas, H.C. Barshilia, Solution combustion synthesis, characterization, magnetic, and dielectric properties of $CoFe_2O_4$ and $Co_{0.5}M_{0.5}Fe_2O_4$ (M = Mn, Ni, and Zn), *Phys. Chem. Chem. Phys.* 22 **(2020)** 20087–20106. https://doi.org/10.1039/d0cp03161e.

[17]   D. Rajan Babu, K. Venkatesan, Synthesis of nanophasic $CoFe_2O_4$ powder by self-igniting solution combustion method using mix up fuels, *J. Cryst. Growth* 468 **(2017)** 179–184.

https://doi.org/10.1016/j.jcrysgro.2016.11.054.

[18] A. Fujimori, K. Ohmura, N. Honda, K. Kakizaki, Creation of High-Density and Low-Defect Single-Layer Film of Magnetic Nanoparticles by the Method of Interfacial Molecular Films, *Langmuir* 31 **(2015)** 3254–3261. https://doi.org/10.1021/acs.langmuir.5b00241.

[19] A. Thampi, K. Babu, S. Verma, Large scale solvothermal synthesis and a strategy to obtain stable Langmuir-Blodgett film of $CoFe_2O_4$ nanoparticles, *J. Alloys Compd.* 564 **(2013)** 143–150. https://doi.org/10.1016/j.jallcom.2013.02.139.

[20] I. Haïk Dunn, S.E. Jacobo, P.G. Bercoff, Structural and magnetic influence of yttrium-for-iron substitution in cobalt ferrite, *J. Alloys Compd.* 691 **(2017)** 130–137. https://doi.org/10.1016/j.jallcom.2016.08.223.

[21] J.D. Zuluaga-Parra, S. Sánchez-Valdés, L.F. Ramos-deValle, F.I. Beltrán-Ramírez, L. Da-Silva, E. Ramírez-Vargas, S. Vázquez-Rodríguez, S. Flores-Gallardo, J. Méndez-Nonell, M. Valera-Zaragoza, E.N. Cabrera-Álvarez, A novel method for the modification of magnetite nanoparticles for the enhancement of its dispersibility in hydrophobic media, *J. Magn. Magn. Mater.* 514 **(2020)** 167169. https://doi.org/10.1016/j.jmmm.2020.167169.

[22] V. Daboin, S. Briceño, J. Suárez, L. Carrizales-Silva, O. Alcalá, P. Silva, G. Gonzalez, Magnetic SiO_2-$Mn_{1-x}Co_xFe_2O_4$ nanocomposites decorated with $Au@Fe_3O_4$ nanoparticles for hyperthermia, *J. Magn. Magn. Mater.* 479 **(2019)** 91–98. https://doi.org/10.1016/j.jmmm.2019.02.002.

[23] V.B. Daboin, S.N.M. Betancourt, E.D. Farias, J.S. Riva, P.G. Bercoff, Enhancement of the electrochemical oxygen evolution reaction by light and external magnetic fields, using hybrid electrodes made by Langmuir–Blodgett, *Electrochim. Acta* 480 **(2024)** 143910. https://doi.org/10.1016/j.electacta.2024.143910.

[24] S. Sun, H. Zeng, D.B. Robinson, S. Raoux, P.M. Rice, S.X. Wang, G. Li, Monodisperse MFe_2O_4 (M = Fe, Co, Mn) Nanoparticles, *J. Am. Chem. Soc.* 126 **(2004)** 273–279. https://doi.org/10.1021/ja0380852.

[25] S. Mourdikoudis, R.M. Pallares, N.T.K. Thanh. Characterization techniques for nanoparticles: comparison and complementarity upon studying nanoparticle properties, Nanoscale, 10 **(2018)** 12871-12934. DOI: 10.1039/C8NR02278J.

[26] M.S. Abd El-Sadek1, H.S. Wasly, K.M. Batoo. X-ray peak profile analysis and optical properties of CdS nanoparticles synthesized via the hydrothermal method, Appl. Phys. A, 125 **(2019).** https://doi.org/10.1007/s00339-019-2576-y

[27] S.M. Ansari, R.D. Bhor, K.R. Pai, D. Sen, S. Mazumder, K. Ghosh, Y.D. Kolekar, C. V. Ramana, Cobalt nanoparticles for biomedical applications: Facile synthesis, physiochemical characterization, cytotoxicity behavior and biocompatibility, *Appl. Surf. Sci.* 414 **(2017)** 171–187. https://doi.org/10.1016/j.apsusc.2017.03.002.

[28] P.H. Nam, L.T. Lu, P.H. Linh, D.H. Manh, L.T. Thanh Tam, N.X. Phuc, P.T. Phong, I.J. Lee, Polymer-coated cobalt ferrite nanoparticles: Synthesis, characterization, and toxicity for hyperthermia applications, *New J. Chem.* 42 **(2018)** 14530–14541. https://doi.org/10.1039/c8nj01701h.

[29] Z. Mahhouti, H. El Moussaoui, T. Mahfoud, M. Hamedoun, M. El Marssi, A. Lahmar, A. El Kenz, A. Benyoussef, Chemical synthesis and magnetic properties of monodisperse cobalt ferrite nanoparticles, *J. Mater. Sci. Mater.* Electron. 30 **(2019)** 14913–14922. https://doi.org/10.1007/s10854-019-01863-3.

[30] L. Li, Y. Yang, J. Ding, J. Xue, Synthesis of magnetite nanooctahedra and their magnetic field-induced two-/three-dimensional superstructure, *Chem. Mater.* 22 **(2010)** 3183–3191. https://doi.org/10.1021/cm100289d.

[31] D. Maity, D.C. Agrawal, Synthesis of iron oxide nanoparticles under oxidizing environment and their stabilization in aqueous and non-aqueous media, *J. Magn. Magn. Mater.* 308 **(2007)** 46–55. https://doi.org/10.1016/j.jmmm.2006.05.001.

[32] S. Briceño, P. Silva, W. Bramer-escamilla, J. Zabala, Magnetic water-soluble rhamnose-coated $Mn_{1-x}Co_xFe_2O_4$ nanoparticles as potential heating agents for hyperthermia, *Biointerface Res. Appl. Chem.* 5 **(2015)** 910–915.

[33] H. Zhang, D. Zeng, Z. Liu, The law of approach to saturation in ferromagnets originating from the magnetocrystalline anisotropy, *J. Magn. Magn. Mater.* 322 **(2010)** 2375–2380. https://doi.org/10.1016/J.JMMM.2010.02.040.

[34] B.D. Cullity, C.D. Graham, Introduction to Magnetic Materials, Second Edition - Wiley Online Library, **2008.** http://onlinelibrary.wiley.com/book/10.1002/9780470386323.

[35] I. Sharifi, H. Shokrollahi, S. Amiri, Ferrite-based magnetic nanofluids used in hyperthermia applications, *J. Magn. Magn. Mater.* 324 **(2012)** 903–915. https://doi.org/10.1016/j.jmmm.2011.10.017.

[36] A. Zorai, A. Souici, D. Dragoe, E. Rivière, S. Ouhenia, J. Belloni, M. Mostafavi. Superparamagnetic cobalt ferrite nanoparticles synthesized by gamma irradiation, New J. Chem. 47 **(2023)** 2626-2634. DOI: 10.1039/D2NJ05433G

[37] K. Maaz, A. Mumtaz, S.K. Hasanain, A. Ceylan. Synthesis and Magnetic Properties of Cobalt Ferrite ($CoFe_2O_4$) Nanoparticles Prepared by Wet Chemical Route. J. Magn. Magn. Mater. 308 **(2007)** 289–295. http://dx.doi.org/10.1016/j.jmmm.2006.06.003

[38] K. Gandha, K. Elkins; N. Poudyal, J. P. Liu. Synthesis and characterization of $CoFe_2O_4$ nanoparticles with high coercivity. J. Appl. Phys. 117 **(2015)** 17A736. https://doi.org/10.1063/1.4916544

[39] S.E. Shirsath, X. Liu, Y. Yasukawa, S. Li, A. Morisako, Switching of magnetic easy-axis using crystal orientation for large perpendicular coercivity in $CoFe_2O_4$ thin film, *Sci. Rep.* 6 **(2016)** 30074. https://doi.org/10.1038/srep30074.

[40] F. Eskandari, S.B. Porter, M. Venkatesan, P. Kameli, K. Rode, J.M.D. Coey, Magnetization and anisotropy of cobalt ferrite thin films, *Phys. Rev. Mater.* 1 **(2017)** 074413. https://doi.org/10.1103/PhysRevMaterials.1.074413.

[41] V. Bilovol, L.G. Pampillo, D. Meier, U. Wolff, F. Saccone, Cobalt ferrite films: Nanopolishing and magnetic properties, I*EEE Trans. Magn.* 50 **(2014)** 1–5. https://doi.org/10.1109/TMAG.2014.2316481.

[42] M. Khodaei, S.A. Seyyed Ebrahimi, Y.J. Park, J.M. Ok, J.S. Kim, J. Son, S. Baik, Strong in-plane magnetic anisotropy in (111)-oriented $CoFe_2O_4$ thin film, *J. Magn. Magn. Mater.* 340 **(2013)** 16–22. https://doi.org/10.1016/j.jmmm.2013.03.019.

[43] M.S. Aprea, J.S. Riva, P.G. Bercoff, M. Vázquez, Temperature dependence of magnetic anisotropy in a cylindrical $Fe_{65}Pd_{35}$ nanowire array, *J. Magn. Magn. Mater.* 564 **(2022)** 170166. https://doi.org/10.1016/j.jmmm.2022.170166.

[44] M.H. Carvalho, R.J.S. Lima, C.T. Meneses, W.S.D. Folly, V.H.V. Sarmento, A.A. Coelho, J.G.S. Duque, Determination of the effective anisotropy constant of $CoFe_2O_4$ nanoparticles through the T-dependence of the coercive field, *J. Appl. Phys.* 119 **(2016)** 093909. https://doi.org/10.1063/1.4942535.

[45] T.E. Torres, E. Lima, A. Mayoral, A. Ibarra, C. Marquina, M.R. Ibarra, G.F. Goya, Validity of the Néel-Arrhenius model for highly anisotropic $Co_xFe_{3-x}O_4$ nanoparticles, *J. Appl. Phys.* 118 **(2015)** 183902. https://doi.org/10.1063/1.4935146.

[46] K. Maaz, M. Usman, S. Karim, A. Mumtaz, S.K. Hasanain, M.F. Bertino, Magnetic response of core-shell cobalt ferrite nanoparticles at low temperature, *J. Appl. Phys.* 105 **(2009)** 113917. https://doi.org/10.1063/1.3139293.

[47] E. Della Torre, L.H. Bennett, R.E. Watson, Extension of the Bloch $T^{3/2}$ law to magnetic nanostructures: Bose-Einstein condensation, *Phys. Rev. Lett.* 94 **(2005)** 17A928. https://doi.org/10.1103/PhysRevLett.94.147210.

[48] I.M. Obaidat, C. Nayek, K. Manna, Investigating the role of shell thickness and field cooling on saturation magnetization and its temperature dependence in $Fe_3O_4/\gamma-Fe_2O_3$ core/shell nanoparticles, *Appl. Sci.* 7 **(2017)** 1269. https://doi.org/10.3390/app7121269.

[49] S. Linderoth, L. Balcells, A. Labarta, J. Tejada, P. V. Hendriksen, S.A. Sethi, Magnetization and Mössbauer studies of ultrafine Fe-C particles, *J. Magn. Magn. Mater.* 124 **(1993)** 269–276. https://doi.org/10.1016/0304-8853(93)90125-L.

[50] N.S.E. Osman, T. Moyo, Temperature Dependence of Coercivity and Magnetization of $Sr_{1/3}Mn_{1/3}Co_{1/3}Fe_2O_4$ Ferrite Nanoparticles, *J. Supercond. Nov. Magn.* 29 **(2016)** 361–366. https://doi.org/10.1007/s10948-015-3227-y.

[51] C.Y. Li, S.K. Karna, C.W. Wang, W.H. Li, Spin polarization and quantum spins in Au nanoparticles, *Int. J. Mol. Sci.* 14 **(2013)** 17618–17642. https://doi.org/10.3390/ijms140917618.

[52] P. V. Hendriksen, S. Linderoth, P.A. Lindgård, Finite-size effects in the magnetic properties of ferromagnetic clusters, *J. Magn. Magn. Mater.* 104–107 **(1992)** 1577-1579. https://doi.org/10.1016/0304-8853(92)91461-2.

[53] K. Chakrabarti, B. Sarkar, V.D. Ashok, K. Das, S.S. Chaudhuri, S.K. De, Interfacial magnetism and exchange coupling in $BiFeO_3$-CuO nanocomposite, *Nanotechnology* 24 **(2013)** 505711. https://doi.org/10.1088/0957-4484/24/50/505711.